Onsite and intersite electronic correlations in the Hubbard model for halide perovskites

Jiyuan Yang,[1,2,*] Tianyuan Zhu,[2,3,*] and Shi Liu [2,3,†]

[1]*Zhejiang University, Hangzhou, Zhejiang 310058, China*
[2]*Key Laboratory for Quantum Materials of Zhejiang Province, Department of Physics, School of Science,*
Westlake University, Hangzhou, Zhejiang 310024, China
[3]*Institute of Natural Sciences, Westlake Institute for Advanced Study, Hangzhou, Zhejiang 310024, China*

Halide perovskites (HPs) are widely viewed as promising photovoltaic and light-emitting materials for their suitable band gaps in the visible spectrum. Density functional theory (DFT) calculations employing (semi)local exchange-correlation functionals usually underestimate the band gaps for these systems. Accurate descriptions of the electronic structures of HPs often demand higher-order levels of theory such as the Heyd-Scuseria-Ernzerhof (HSE) hybrid density functional and GW approximations that are much more computationally expensive than standard DFT. Here, we investigate three representative types of HPs, ABX_3 halide perovskites, vacancy-ordered double perovskites, and bond disproportionated halide perovskites (BDHPs), using DFT $+ U + V$ with onsite U and intersite V Hubbard parameters computed self-consistently without *a priori* assumption. The inclusion of Hubbard corrections improves the band gap prediction accuracy for all three types of HPs to a similar level of advanced methods. Moreover, the self-consistent Hubbard U is a meaningful indicator of the true local charge state of multivalence metal atoms in HPs. The inclusion of the intersite Hubbard V is crucial to properly capture the hybridization between valence electrons on neighboring atoms in BDHPs that have breathing-mode distortions of halide octahedra. In particular, the simultaneous convergence of both Hubbard parameters and crystal geometry enables a band gap prediction accuracy superior to HSE for BDHPs but at a fraction of the cost. Our work highlights the importance of using self-consistent Hubbard parameters when dealing with HPs that often possess intricate competitions between onsite localization and intersite hybridization.

I. INTRODUCTION

Halide perovskites (HPs) have drawn intensive interest over the past decade for their remarkable optoelectronic properties and promising photovoltaic applications [1–4]. The suitable and tunable band gap and small charge carrier effective mass of HPs make them excellent candidates for optical absorber materials [5,6]. Since the report of the very first perovskite-based solar cell (PSC) by Kojima *et al.* in 2009, the power conversion efficiencies of PSCs have improved rapidly from 3.8% to 25.5% [1,4]. Despite the high performance and the low fabrication cost of HPs, the intrinsic long-term instability remains a major hurdle impeding the commercialization of PSCs [7,8]. In addition, the presence of toxic elements such as lead (Pb) raises concerns regarding the environmental and health impacts of large-scale deployment of Pb-based PSCs [9,10]. All these issues have prompted the scientific community to search for different types of perovskite derivatives [11].

The prototypical HP has a general chemical formula of ABX_3, where A is a monovalent organic or inorganic cation (e.g., $CH_3NH_3^+$ and Cs^+), B is a divalent metal cation (e.g., Pb^{2+} and Sn^{2+}), and X is a halide anion (e.g., I^-, Br^-, and Cl^-). The ABX_3 structure consists of a corner-sharing BX_6

octahedra network with the A-site cations locating in the cavities between adjacent octahedra [Fig. 1(a)]. To address the long-term instability issue of $CsSnI_3$ in which Sn adopts a formal oxidation state of 2+, Lee *et al.* introduced Cs_2SnI_6, a vacancy-ordered double halide perovskite (VODP), that has Sn adopting the 4+ formal oxidation state and is stable in air and moisture [12]. The VODP is derived from the ABX_3 HPs by removing every other B-site cations [Fig. 1(b)], and hence has a chemical formula of A_2BX_6 [13,14]. By forming vacancies at half of the B sites, the nominal oxidation state of B changes from 2+ in ABX_3 to 4+ in A_2BX_6. Since then, various types of VODPs such as Cs_2BX_6 ($B =$ Sn, Te, Ti, Zr, Pd, Pt) in which the B site is occupied by metals with stable oxidation state of 4+ have been synthesized [15–24].

Some HPs such as $CsAuCl_3$ [25] and $CsTlF_3$ [26] possess so-called breathing-mode distortions of halide octahedra where BX_6 cages are alternately dilated and contracted in a rocksalt-like pattern [Fig. 1(c)]. The breathing structural distortions were originally attributed to the charge disproportionation of B-site cations, $2B^{2+} \rightarrow B^+ + B^{3+}$, that leads to two different sets of B-X bond lengths [27–29]. This type of structural flexibility enriches the optical and electronic properties of halide perovskites such as high-T_C superconductivity and semiconductor-to-metal phase transition [26,29–31]. Recently, such charge-ordering picture was challenged both theoretically and experimentally [32–34]. For example, investigations based on density functional theory (DFT) calculations indicated that the physical charges of B-site cations

---
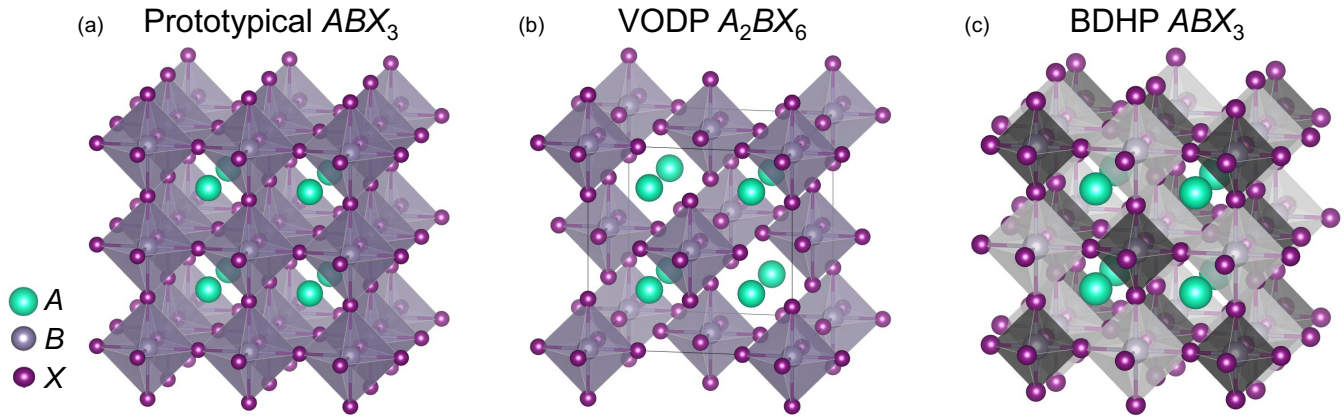[*]These two authors contributed equally to this paper.
[†]liushi@westlake.edu.cn

FIG. 1. Schematics of three types of halide perovskites. (a) Prototypical ABX_3 HP, (b) A_2BX_6 VODP, and (c) ABX_3 BDHP.

in $CsAuCl_3$ remain largely unchanged despite being in different local environments [33,34]. This is due to the "charge self-regulating response" [32] in which B-site metal atoms and X ligands rehybridize to prevent the creation of highly charged cations through the ligand-to-metal charge transfer. For this reason, it was proposed to describe these ABX_3 HPs as "bond disproportionated" (BD) instead of "charge ordered." Similarly, it was found that the actual charge density residing on the Sn atom in $CsSnI_3$ and Cs_2SnI_6 is nearly identical although Sn adopts different formal oxidation states in these two compounds [35].

An accurate description of the electronic structures of different types of HPs is vital for the rational design and optimization of HP-based photovoltaic and optoelectronic devices. DFT has played an important role in the discovery and design of HPs [6,36–38]. However, the accuracy of DFT is limited by the approximations to the exchange-correlation energy functional. The remnant self-interaction error (SIE) [39] within the local-density approximation [40] and generalized gradient approximation (GGA) [41] often causes a considerable underestimation of band gaps in systems with localized electronic states (e.g., 3d electrons). It is noted that when the B site is occupied by heavy elements such as Pb, the inclusion of the spin-orbit coupling (SOC) effects in DFT calculations can significantly reduce the theoretical band gap values [36]. As a result, there exists a notable error cancellation when using GGA without SOC to evaluate the band gaps of Pb-based HPs [37,38]. Advanced methods such as the GW approximation and the Heyd-Scuseria-Ernzerhof (HSE) hybrid density functional are more accurate, but their expensive computational costs often limit the applications to small systems of tens of atoms.

The DFT + U method based on the mean-field Hubbard model that removes SIE is a cost-effective way to improve the descriptions of electronic correlations [42]. Specifically, the Hubbard energy approximates derivative discontinuities [43] and enforces the piecewise linearity of the total energy with respect to occupation numbers for states in the Hubbard manifold [44]. The Hubbard parameter U gauges the strength of the onsite (screened) Coulomb repulsion of localized electrons and is critical for the accuracy of DFT + U. In many studies, the value of U is assumed to be element-specific and is manually tuned to reproduce experimental results and/or

results from higher-order levels of theory. It is highly desirable to determine U in an unbiased way with minimum human intervention. In order to address this problem, Agapito et al. formulated a pseudohybrid Hubbard density functional, Agapito-Curtarolo-Buongiorno Nardelli (ACBN0), enabling a direct self-consistent computation of Hubbard U parameters [45]. By further including the Coulomb interactions between electrons on nearest-neighboring Hubbard sites [46] (denoted as intersite V), Lee et al. and Tancogne-Dejean et al. respectively developed an extended version of ACBN0, termed eACBN0, that enables a fully ab $initio$ DFT + U + V method using self-consistent onsite U and intersite V parameters [47,48]. In addition, the common practice to apply U corrections only to partially filled and localized d and f states is based on the assumptions that (a) those d and f states contribute the most to the Hubbard energy and (b) s and p states are likely more diffusive such that they are already well described by conventional exchange-correlation functionals like PBE. However, these assumptions, in our opinion, should not be regarded as "universal principles." When the valence states near the Fermi level are dominated by s- and/or p-orbital characters, it is justified to apply U corrections to those states based on the definition of Hubbard energy [45].

It is desirable to develop a fully ab $initio$ and computationally affordable approach to accurately predict the electronic structures of HPs. In this work, by employing ACBN0 and eACBN0, we perform an extensive investigation on the electronic structures of three different types of HPs: prototypical ABX_3 HPs, A_2BX_6 VODPs, and ABX_3 BDHPs, as sketched in Fig. 1. We compare the band gap values with those obtained in experiments and calculated by HSE and GW methods (if available), and find that the self-consistent Hubbard U and V parameters affect the electronic structures of HPs to different degrees depending on the chemical bonding nature. For prototypical ABX_3 HPs, the DFT + U method with U computed with ACBN0 is sufficiently accurate, yielding band gap values at the GW level; the intersite V, however, has limited impacts on the band structures. As regards VODPs, both U and V play significant roles, with DFT + U correcting the band gap values to the HSE level and DFT + U + V further to the G_0W_0 level. In the case of BDHPs, we discover canceling effects when applying U corrections to different localized states and the inclusion of the intersite Hubbard V is crucial to capture

the hybridization between valence electrons on neighboring Hubbard sites. Finally, we demonstrate that the simultaneous convergence of both Hubbard parameters and crystal geometry enables a band gap prediction accuracy superior to HSE for BDHPs.

II. COMPUTATIONAL METHODS

We perform standard DFT calculations with QUANTUM ESPRESSO (QE) [49,50] using GGA of the Perdew-Burke-Ernzerhof (PBE) parametrization [41]. Ultrasoft pseudopotentials taken from the Garrity-Bennett-Rabe-Vanderbilt (GBRV) library [51] are used for structural optimizations. For all inorganic HPs, we fully optimize both the lattice constants and atomic positions. In the case of organic-inorganic hybrid HPs such as $CH_3NH_3PbI_3$, since the lattice constants optimized with the zero-kelvin DFT method often depend on *a priori* orientational ordering of molecular cations, we decide to only relax the atomic positions with lattice constants fixed to experimental values. We use an energy convergence threshold of 10^{-7} Ry, a force convergence threshold of 10^{-6} Ry/bohr, and a plane wave cutoff energy of 50 Ry to obtain the ground-state structures. An $8 \times 8 \times 8$ k-point mesh is used for cubic HPs, and the k-point mesh is modified accordingly for other phases to maintain a similar k-point density. For VODPs and BDHPs, a $4 \times 4 \times 4$ k-point mesh is used. Then based on PBE optimized structures, we compute U and V parameters with ACBN0 and eACBN0 using an in-house version of QE [47] and GBRV pseudopotentials. The threshold for the convergences of U and V values is set as 10^{-6} Ry of Hubbard energy. Kirchner-Hall and coworkers calculated the onsite Hubbard U parameters with first-principles density functional perturbation theory for 20 compounds containing transition-metal or p-block elements and found that the orthogonalized projectors gave the most accurate band gaps [52]. Here, we also use orthogonalized projectors (*ortho-atomic* orbitals as implemented in QE) for DFT $+ U$ calculations.

To include the SOC effects on the band gaps, fully relativistic optimized norm-conserving pseudopotentials provided by the PseudoDoJo project [53] are chosen, and an increased plane wave cutoff energy of 80 Ry is used to compute the band gaps. Because current implementation of DFT $+ U + V$ in QE does not support fully relativistic pseudopotentials, the SOC-induced band gap correction in eACBN0+SOC is approximated as $\Delta_{SOC} = E_g(DFT + U + SOC) - E_g(DFT + U)$, where the values of U in DFT $+ U$ are computed self-consistently with ACBN0. That is, for a given HP, we assume the magnitudes of Δ_{SOC} in ACBN0+SOC and eACBN0+SOC are the same. For DFT $+ U$ and DFT $+ U + V$ calculations, we employ the simplified rotationally invariant formulation [54], and the atomic orbitals orthogonalized using Löwdin's method [55,56] are adopted to construct projectors of the Hubbard manifold. The same settings of DFT $+ U + V$ are used in the sc-eACBN0 loop (see later discussions) to converge both geometry and Hubbard parameters at the same time. The sc-eACBN0 calculation reaches the convergence when the changes in Hubbard parameters are less than 10^{-4} Ry. All structural files of optimized structures and representative input files for DFT $+ U$ and DFT $+ U + V$ calculations are uploaded to public repositories [57,58].

TABLE I. Self-consistent U and V values (in eV) for different orbitals in $CsSnI_3$ and Cs_2SnI_6 computed with ACBN0 and eACBN0 using the ground-state structures optimized with PBE. V_{sp} is the intersite Hubbard term between nearest-neighboring Sn-5s and I-5p; V_{pp} is for intersite interactions between Sn-5p and I-5p. Underlined Hubbard parameters are most important for band gap predictions.

	$CsSnI_3$		Cs_2SnI_6	
	ACBN0	eACBN0	ACBN0	eACBN0
U(Cs-6s)	0.01	0.01	0.10	0.10
U(Cs-5p)	5.80	5.67	6.45	6.42
U(Sn-5s)	2.37	2.26	1.59	1.05
U(Sn-5p)	0.10	0.14	0.13	0.15
U(I-5s)	9.75	9.81	9.34	9.26
U(I-5p)	4.08	4.07	4.46	4.40
V_{sp}		1.60		1.18
V_{pp}		1.57		1.67

III. RESULTS AND DISCUSSION

A. Electronic structures of prototypical *ABX*$_3$ HPs

It is common to apply Hubbard corrections to strongly localized d and f electrons [59–61], though recent investigations highlighted the importance of applying U corrections to also s and p states [47,48,62,63]. In practice, the construction of the Hubbard manifold, namely the orbitals on which the Hubbard Hamiltonian will act, is largely based on empirical rules or intuition. Here, taking $CsSnI_3$ as an example, we compute Hubbard parameters with ACBN0 for multiple orbitals at the same time: Sn-5s, Sn-5p, I-5s, I-5p, Cs-6s, and Cs-5p. The self-consistent U values are reported in Table I. The magnitude of U in ACBN0 depends on the degree of localization of the Bloch states because of the introduction of the renormalized density matrix, which makes sure that ACBN0 reduces to PBE for delocalized states that are already properly described by PBE [45]. This is indeed the case for Cs-6s and Sn-5p states; both have nearly zero U values. In comparison, the onsite U for the Sn-5s states in $CsSnI_3$ acquires a nonnegligible magnitude of 2.37 eV, an indication of appreciable electronic correlation effects of lone-pair 5s electrons of Sn. These results demonstrate that a self-consistent approach that naturally picks up important orbitals to construct the Hubbard manifold is capable of reducing the bias due to an *ad hoc* orbital selection.

A detailed analysis is performed to diagnose the effects of the Hubbard U on the electronic structure of $CsSnI_3$ by comparing the results obtained with Hubbard manifolds of different constituent local states. The PBE band structure and projected density of states (PDOS) are shown in Fig. 2(a), revealing that the valance-band edge is predominantly of I-5p character with small Sn-5s hybridization while the conduction-band edge takes almost exclusively a Sn-5p character. The isolated single band between -6 and -8 eV is from Sn-5s and I-5p states. PBE gives a direct band gap of 0.40 eV at Γ, much lower than the experimental value of 1.3 eV. After applying a Hubbard U correction of 2.37 eV to Sn-5s states [denoted as DFT $+ U_s$(Sn)], the band gap increases to 0.78 eV, due to a rigid downshift of the top of the

(a)

PBE

(b)

DFT+U: {U_s(Sn)}

(c)

DFT+U: {U_p(I)}

(d)

DFT+U: {U_s(Sn), U_p(I)}
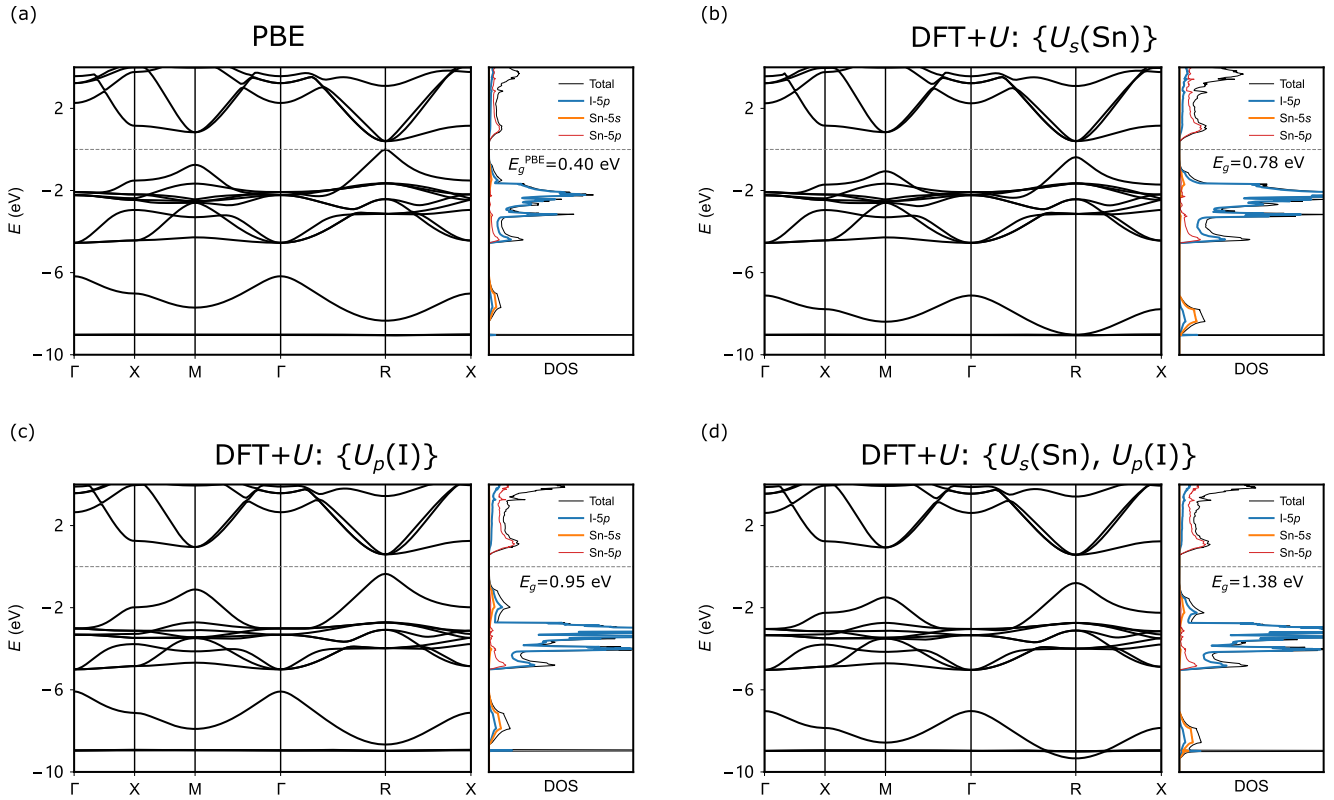

FIG. 2. Diagnostic analysis of Hubbard U corrections in $CsSnI_3$. Comparison between the band structures and projected density of states (DOS) computed with (a) PBE, (b) ACBN0 with Hubbard U applied to Sn-5s states, (c) ACBN0 with Hubbard U applied to I-5p states, and (d) ACBN0 with U corrections applied to both Sn-5s and I-5p states. U values are reported in Table I. All band structures have the core energies aligned and use the same absolute energy as the Fermi level to show the band shifting resulting from U corrections.

valence manifold [Fig. 2(b)]. Given the small contribution of Sn-5s states to the valance-band edge, the improved band-gap prediction resulting from U_s(Sn) seems puzzling. We find that the use of U_s(Sn) downshifts the single band between -6 and -8 eV such that the s-p repulsion between this low-lying band of substantial Sn-5s character and the I-5p bands that dominate the valence-band edge is reduced, eventually leading to the downshift of the valance band maximum (VBM). A similar gap opening mechanism was also found in ZnO [45]. It was shown that applying U corrections to low-lying Zn-3d states would reduce the p-d repulsion between Zn-3d and O-2p bands, which in turn lowered the energy of the valance band maximum and increased the band gap. We note that as U_s(Sn) is computed self-consistently in ACBN0, the observed reduction of s-p repulsion is likely a genuine manifestation of the correlation effect of the $5s^2$ lone pair of Sn despite the common belief that lone-pair electrons are inactive. Applying an onsite Coulomb potential to 5p electrons on I sites alone [denoted as DFT + U_p(I)] also increases the band gap to 0.95 eV, ascribed to the downshift of I-5p bands [Fig. 2(c)]. Though DFT + U_s(Sn) and DFT + U_p(I) give comparable band gap values (0.78 versus 0.95 eV), their PDOS spectra are notably different. Specifically, the PDOS between -6 and 0 eV obtained with DFT + U_p(I) splits into two regions with a minor peak at -2 eV; such splitting is absent in the PDOS spectrum computed with DFT + U_s(Sn). The change in PDOS near the Fermi level (E_F) will likely impact the elec-

tronic transport properties such as carrier mobility. Finally, the concomitant use of U_s(Sn) and U_p(I) increases the band gap to 1.38 eV, agreeing well with the experimental value of 1.3 eV. Because bands of Cs-5p and I-5s characters are low-dispersion deep levels, applying U corrections to these semicore states has little impact on states near E_F and the band gap.

We further consider intersite Hubbard interactions between nearest-neighboring Hubbard sites with V parameters computed self-consistently with eACBN0. It is noted that eACBN0 also evaluates all on-site Hubbard parameters on-the-fly, and the U values obtained with ACBN0 and eACBN0 are comparable (Table I). The self-consistent V parameter corresponding to the hybridization between valence 5s and 5p electrons of nearest-neighboring Sn and I atoms is ≈ 1.6 eV. Interestingly, as illustrated in Fig. 3, the inclusion of this intersite V correction does not alter the band gap or the band dispersion: ACBN0 and eACBN0 band structures match closely with each other. As we will discuss in detail below, the electronic structure of $CsSnI_3$ is insensitive to Hubbard V corrections due to the antibonding nature of VBM.

A series of calculations are performed to explore the accuracy of ACBN0 and eACBN0 methods for a list of ABX_3 HPs and their polymorphs (α = cubic, γ = orthorhombic, and t = tetragonal) with known experimental band gaps. Based on above detailed investigations on $CsSnI_3$, the Hubbard U corrections are applied B-site s states and X-site p states. The
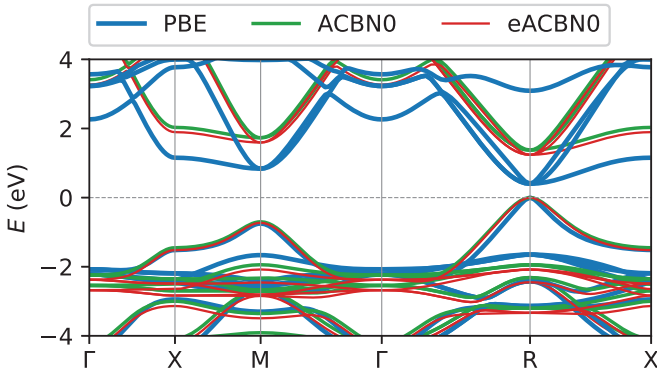
FIG. 3. Comparison of the band structures of $CsSnI_3$ obtained with PBE, ACBN0, and eACBN0, respectively. The valence band maximum is set as the Fermi level.

states of A-site atoms contribute little to band edges, thus being excluded from the Hubbard manifold. The intersite V between s electrons on B sites and p electrons centered on nearest-neighboring X sites is considered in eACBN0. The band gaps are tabulated in Table II and plotted in Fig. 4.

For Sn-based HPs, PBE, with a mean absolute error (MAE) of 1.01 eV, substantially underestimates the band gap values with reference to experimental results [Fig. 4(a)]. Both ACBN0 and eABNC0 improve the band gap predictions upon

PBE, and their MAEs are 0.37 and 0.36 eV, respectively. The nearly identical MAEs of ACBN0 and eACBN0 indicate the intersite V interactions are not essential in these HPs. We note that this reflects a good feature of eACBN0: It reduces to ACBN0 when the electronic structure is already properly described without including intersite V. Additionally, the inclusion of SOC only reduces the band gap slightly for Sn-based HPs [Fig. 4(b)]: the average band gap reduction is 0.32 eV for HPs containing I, 0.27 eV for Br, and 0.24 eV for Cl. In general, both ACBN0+SOC (MAE = 0.38 eV) and eACBN0+SOC (MAE = 0.44 eV) are more accurate than HSE+SOC (MAE = 0.61 eV), while GW+SOC appears to be the most reliable (MAE = 0.18 eV). We find that for α-$CsSnCl_3$ and α-$MASnCl_3$, the band gaps predicted by eACBN0+SOC (1.81 and 2.26 eV), though being much better than those predicted with PBE+SOC (0.57 and 1.46 eV), remain much lower than experimental values (2.9 and 3.69 eV). Actually, the GW values (2.70 and 3.44 eV) are also slightly smaller than experimental values. Considering that eACBN0 is essentially a mean field approach, it is not that surprising that this method may show its own limitation in some cases, being less accurate than the GW method that is based on many-body perturbation theory.

In the case of Pb-based HPs, PBE achieves a good agreement with experimental data due to fortuitous error cancellations in the absence of SOC. As expected, the band gap

TABLE II. Comparison of the band gaps (in eV) as computed with different methods and as measured in experiments for prototypical ABX_3 HPs. The mean absolute error (MAE) of each method is computed for Sn-based HPs and Pb-based HPs separately; MAE_t reflects the accuracy for all ABX_3 HPs.

|	This Work						Reference		
	Without SOC			With SOC					
ABX_3	PBE	ACBN0	eACBN0	PBE	ACBN0	eACBN0	HSE+SOC	GW+SOC	Expt.
γ-$CsSnI_3$	0.81	1.68	1.61	0.48	1.36	1.29	1.13 [38]	1.3 [72]	1.3 [73]
Y-$CsSnI_3$	2.06	2.97	2.95	1.90	2.83	2.81		2.7 [72]	2.55 [73]
β-$CsSnBr_3$	0.79	1.91	1.83	0.54	1.72	1.64		1.740 [72]	1.8 [74]
α-$CsSnI_3$	0.40	1.38	1.24	0.005	1.00	0.86	0.82 [38]	1.008 [72]	1.3 [35]
α-$CsSnBr_3$	0.57	1.70	1.61	0.22	1.42	1.33	1.09 [38]	1.382 [72]	1.75 [75]
α-$CsSnCl_3$	0.92	2.12	2.05	0.57	1.88	1.81	1.42 [38]	2.693 [72]	2.9 [76]
t-$MASnI_3$	0.57	1.47	1.35	0.30	1.15	1.03	1.11 [38]	1.10 [77]	1.2 [78]
γ-$MASnI_3$	0.75	1.64	1.53	0.45	1.28	1.17	1.38 [38]		1.20 [79]
α-$MASnI_3$	0.55	1.45	1.34	0.22	1.06	0.95	0.92 [38]	1.03 [80]	1.15 [81]
α-$MASnBr_3$	0.83	1.95	1.83	0.52	1.61	1.49	1.4 [38]	1.90(GW) [82]	2.15 [82]
α-$MASnCl_3$	1.68	2.62	2.50	1.46	2.38	2.26	2.25 [38]	3.44(GW) [82]	3.69 [82]
MAE	1.01	0.37	0.36	1.30	0.38	0.44	0.61	0.18	
γ-$CsPbI_3$	1.83	2.86	2.84	0.74	1.67	1.65	1.75 [38]	1.57 [83]	1.72 [84]
δ-$CsPbI_3$	2.52	3.55	3.54	1.87	2.75	2.74	2.64 [85]		2.82 [86]
α-$CsPbI_3$	1.48	2.54	2.50	0.21	1.22	1.18	1.25 [38]	1.14 [83]	1.73 [84]
α-$CsPbBr_3$	1.78	3.31	3.28	0.56	2.06	2.03	1.64 [38]	2.30 [87]	2.36 [88]
α-$CsPbCl_3$	2.21	3.85	3.84	0.97	2.62	2.61	2.18 [38]	3.03 [87]	3.0 [88]
t-$MAPbI_3$	1.70	2.75	2.69	0.60	1.49	1.43	1.45 [38]	1.67 [77]	1.55 [89]
γ-$MAPbI_3$	1.76	2.76	2.71	0.72	1.52	1.47	1.74 [38]		1.633 [90]
α-$MAPbI_3$	1.61	2.66	2.59	0.44	1.34	1.27	1.32 [38]	1.675 [91]	1.55 [92]
α-$MAPbBr_3$	1.98	3.27	3.19	0.82	1.97	1.89	1.81 [38]	2.55 [93]	2.24 [92]
α-$MAPbCl_3$	2.48	3.80	3.73	1.28	2.49	2.42	2.41 [38]	3.49 [93]	2.97 [92]
MAE	0.31	0.98	0.93	1.34	0.24	0.29	0.37	0.24	
MAE_t	0.68	0.66	0.63	1.32	0.31	0.37	0.48	0.21	
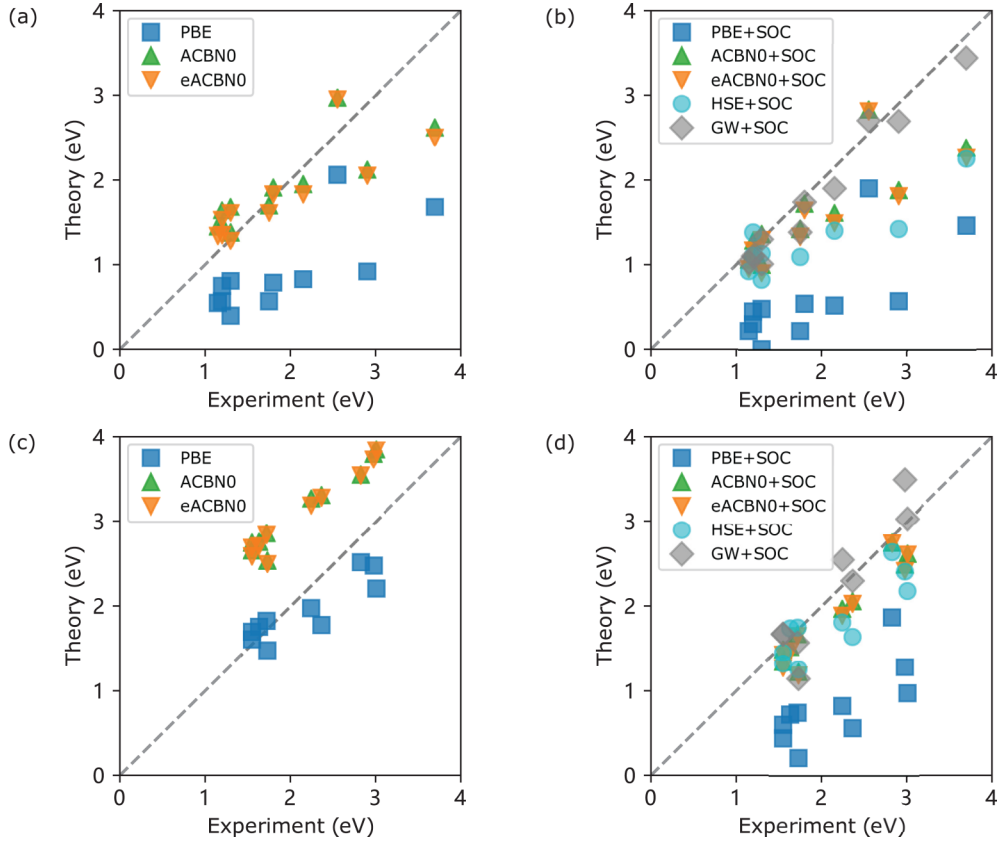
FIG. 4. Comparison of experimental and theoretical band gaps computed with different methods for Sn-based HPs (a) without and (b) with SOC, and for Pb-based HPs (c) without and (d) with SOC.

values obtained with PBE+SOC become much smaller and deviate significantly from experimental values [Fig. 4(d)], leading to a large MAE of 1.34 eV. The band gap reduction due to SOC is 1.11 eV. In comparison, ACBN0+SOC and eACBN0+SOC using self-consistent Hubbard parameters all improve upon PBE+SOC and demonstrate satisfying predictive power, a MAE of 0.24 eV for the former and 0.29 eV for the latter. In summary, it is important to include SOC for HPs containing Pb, and both ACBN0+SOC and eACBN0+SOC have consistent accuracy for *all* studied ABX_3-type HPs but are much more affordable than HSE+SOC and GW+SOC.

B. Electronic structures of A_2BX_6 VODPs

As a typical VODP, Cs_2SnI_6 has Sn adopting a formal oxidation state of +4, which has been used to explain its enhanced stability relative to $CsSnI_3$ [12]. However, Xiao *et al.* [13] pointed out that the Sn ion in Cs_2SnI_6 also adopts a +2 oxidation state where $[SnI_6]^{2-}$ is better understood as $\{Sn^{2+} + [I_6^{6-}L_2^{2+}]^{4-}\}$ with L_2^{2+} representing two holes (L^+) localized on ligand atoms. Dalpian *et al.* [35] used the mechanism of "self-regulating response" (SRR) [32] to explain the relationship between formal oxidation state and the actual charge density residing on the Sn atom: The holes introduced by B-site vacancies are absorbed by the whole system through self-consistent metal-ligand rehybridization. Specifically, DFT calculations revealed that the Sn atom in Cs_2SnI_6 loses 0.6 electrons of 5s character but gains 0.2 5p electrons such that the charge density residing on Sn

is almost unchanged compared to that in $CsSnI_3$. Table I reports the self-consistent Hubbard parameters for Cs_2SnI_6 computed with ACBN0. The Hubbard U for Sn-5s in Cs_2SnI_6 is 1.59 eV, slightly smaller than U_s(Sn) of 2.37 eV in $CsSnI_3$. This supports the SRR mechanism since the magnitude of self-consistent U in ACBN0 is proportional to the occupancy of the localized orbital; if Sn loses all 5s electrons and becomes +4, U_s(Sn) would be nearly zero. Therefore, the self-consistent onsite U could serve as a direct measurement of the local charge state.

An important consequence of metal-ligand rehybridization in Cs_2SnI_6 is that Sn-5s now has no substantial contribution to the VBM but becomes important at the conduction band minimum (CBM), as shown in Fig. 5(a). We perform a diagnostic analysis to comprehend the impacts of onsite U corrections applied to different local orbitals using self-consistent U determined from ACBN0. In reference to a PBE band gap of 0.18 eV, applying the Hubbard U to Sn-5s states actually pushes down the CBM and decreases the band gap slightly to 0.11 eV [Fig. 5(b)]. Because I-5p states dominate the top of the valence-band manifold, the inclusion of U_p(I) downshifts the valence-band edge [Fig. 5(c)] and gives a band gap of 1.03 eV. The concomitant use of U_s(Sn) and U_p(I) yields a band gap of 0.96 eV, agreeing reasonably well with the experimental value of 1.26 eV. It is noted that in some previous studies, the percentage (α) of Hartree-Fock exact exchange in HSE is adjusted to reproduce the experimental band gap [13,18]. For Cs_2SnI_6, HSE with $\alpha = 0.25$ predicts a band gap of 0.93 eV, while HSE with $\alpha = 0.34$ gives a band
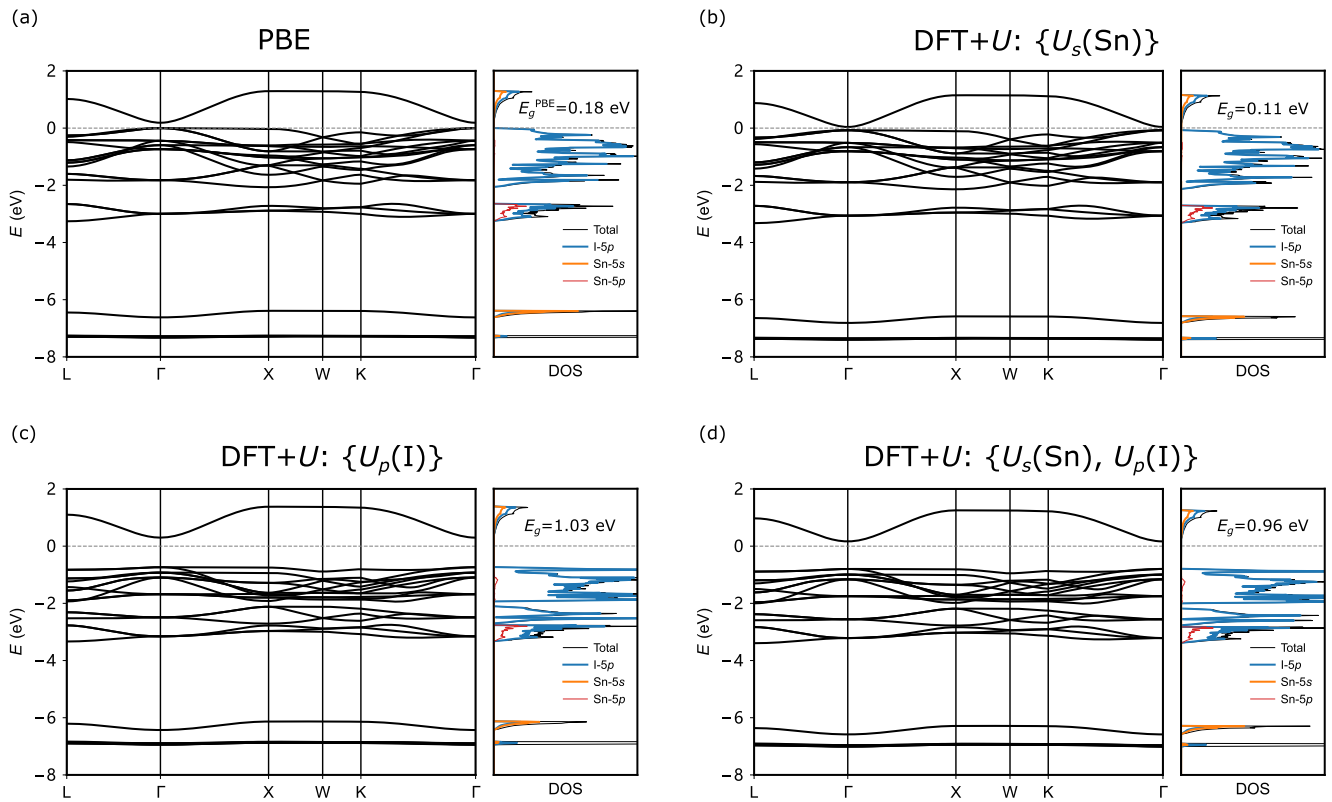
FIG. 5. Diagnostic analysis of Hubbard U corrections in Cs_2SnI_6. Comparison between the band structures and projected density of states (DOS) computed with (a) PBE, (b) ACBN0 with Hubbard U applied to Sn-5s states, (c) ACBN0 with Hubbard U applied to I-5p states, and (d) ACBN0 with U corrections applied to both Sn-5s and I-5p states. U values are taken from Table I. All band structures have the core energies aligned and use the same absolute energy as the Fermi level to show the band shifting resulting from U corrections.

gap of 1.26 eV. In contrast, ACBN0 is fully *ab initio* without tuning parameters. The band gap of Cs_2SnI_6 is found to be insensitive to SOC; for example, PBE and PBE+SOC predict a band gap of 0.18 and 0.13 eV, respectively.

Interestingly, unlike ABX_3 HPs that have band gap values insensitive to V corrections, the band gap of Cs_2SnI_6 increases to 1.42 eV when the intersite Hubbard V interactions between nearest-neighboring Sn-5s and I-5p orbitals are included. We find that ACBN0 and eACBN0 band structures have similar band dispersions, and the effect of Hubbard V corrections in eACBN0 is mainly manifested as a more pronounced upshift of the conduction-band manifold (Fig. 6). As will be detailed below, the band gap of Cs_2SnI_6 opens up monotonically with increasing magnitude of V.

Figure 7 and Table III compare the PBE, ACBN0, and eACBN0 band gaps with HSE values taken from the literature for a few VODPs with known experimental results. The consideration of SOC only slightly reduces the band gap by 0.19 eV for compounds containing I, 0.12 eV for Br, and a negligible amount for Cl. We find that ACBN0+SOC with a MAE of 0.22 eV is much more accurate than PBE+SOC with a MAE of 0.81 eV, and is comparable with HSE that has a MAE of 0.19 eV. Unexpectedly, eACBN0+SOC turns out to be less accurate (MAE = 0.75 eV) and often overestimates the band gap. Despite this seemingly worsened performance, we find that the band gaps predicted by eACBN0 are similar to those obtained with the non-self-consistent many-body

GW method, G_0W_0, that accounts for dynamical screening. Specifically, G_0W_0+SOC predicts the band gaps of Cs_2TiI_6, Cs_2ZrI_6, Cs_2TiBr_6, and Cs_2ZrBr_6 as 2.31, 3.32, 3.87, and 5.02 eV [64], and eACBN0+SOC gives 2.27, 3.05, 3.35, and 4.43 eV, respectively, all higher than HSE values of 1.20, 2.58, 2.01, and 3.88 eV and available experimental data. Previous studies showed that the GW/G_0W_0 approximation yields particularly large errors for materials exhibiting shallow d states,
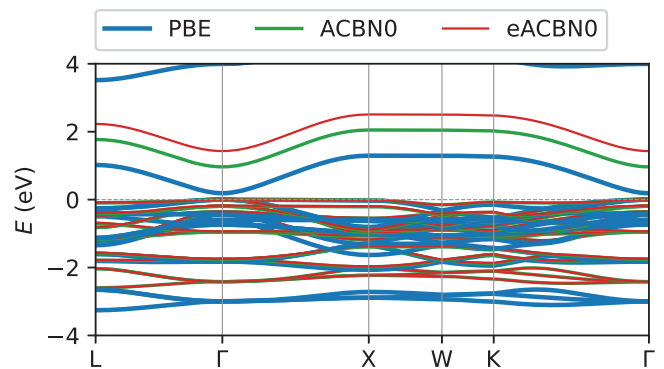

FIG. 6. Comparison of the band structures of Cs_2SnI_6 obtained with PBE, ACBN0, and eACBN0, respectively. The valence band maximum is set as the Fermi level.
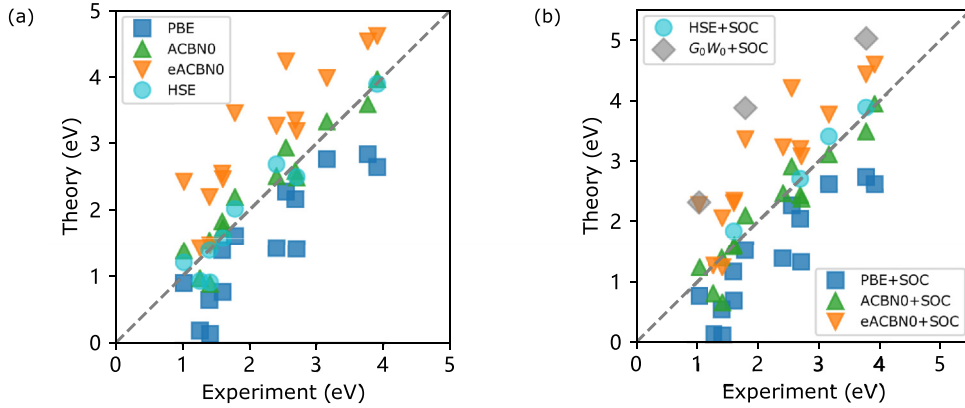
FIG. 7. Comparison of experimental and theoretical band gaps computed with different methods for A_2BX_6 VODPs (a) without and (b) with SOC.

mostly due to the neglect of the attractive interaction between electrons and holes [65–68]. Given the presence of ligand holes in VODPs, the observed band gap overestimation of eACBN0 is not surprising. Therefore, a possible remedy is to include electron-hole interactions in eACBN0 calculations (if possible). Nevertheless, we argue that eACBN0 is principally a more reliable method with accuracy on par with G_0W_0, but in the case of VODPs, the "trick" of error cancellation in ACBN0 (and HSE) somehow works out better than eACBN0 and G_0W_0. It was also suggested that this is because VODPs are not defect tolerant such that the presence of in-gap defect states could strongly affect the measurement that gives an experimental band gap lower than the intrinsic forbidden gap. This could also explain the "overestimation" of eACBN0 for VODPs.

C. Effects of Hubbard V interactions in ABX_3 and A_2BX_6 HPs

We perform a set of model calculations to understand the effects of Hubbard V interactions on the band gaps of $CsSnI_3$ and Cs_2SnI_6 by gradually increasing the magnitude of V parameters between nearest-neighboring Sn-$5s$ and I-$5p$ orbitals. As shown in Fig. 8(a), the band gap of $CsSnI_3$ decreases linearly with increasing V while the band gap of Cs_2SnI_6 increases monotonically. Such opposite V dependence of the band gap in these two different types of HPs can be understood using the energy level diagrams [Figs. 8(b) and 8(c)]. Before the hybridization, I-$5p$ states have higher energy than Sn-$5s$ states. The hybridization leads to the splitting between the bonding and antibonding bands. This is the case for both $CsSnI_3$ and Cs_2SnI_6. In $CsSnI_3$, both bonding and

TABLE III. Comparison of the band gaps (in eV) as computed with different methods and as measured in experiments for A_2BX_6 VODPs.

| | This Work | | | | | | Reference | |
| | Without SOC | | | With SOC | | | | |
A_2BX_6	PBE	ACBN0	eACBN0	PBE	ACBN0	eACBN0	HSE(SOC)	Expt.
Cs_2SnI_6	0.18	0.96	1.42	0.13	0.80	1.26	0.92 [35]	1.26 [12]
Cs_2SnBr_6	1.41	2.48	3.18	1.32	2.37	3.07	2.49 [35]	2.7 [15]
Cs_2SnCl_6	2.64	3.96	4.61	2.61	3.94	4.59	3.89 [35]	3.9 [15]
Cs_2TeI_6	1.39	1.82	2.54	1.16	1.58	2.30	1.83 (SOC) [16]	1.59 [16]
Cs_2TeBr_6	2.16	2.58	3.34	2.04	2.43	3.19	2.7[a] (SOC) [17]	2.68 [17]
Cs_2TeCl_6	2.76	3.32	3.98	2.61	3.10	3.76	3.4[a] (SOC) [17]	3.15 [17]
Cs_2TiI_6	0.89	1.38	2.42	0.76	1.23	2.27	1.20 ($\alpha = 0.16$) [18]	1.02 [18]
Cs_2TiBr_6	1.60	2.19	3.45	1.52	2.09	3.35	2.01 ($\alpha = 0.16$) [18]	1.78 [18]
Cs_2TiCl_6	2.27	2.93	4.23	2.26	2.90	4.20		2.54 [19]
Cs_2ZrI_6	1.83	2.40	3.24	1.65	2.21	3.05	2.58 (SOC) [64]	
Cs_2ZrBr_6	2.83	3.58	4.53	2.73	3.48	4.43	3.88 (SOC) [64]	3.76 [20]
Cs_2PdI_6	0.13	0.88	1.46	0.11	0.65	1.23	0.90 [94]	1.41 [21]
Cs_2PdBr_6	0.76	1.72	2.46	0.68	1.60	2.34	1.57 [23]	1.6 [22]
Cs_2PdCl_6	1.42	2.50	3.26	1.38	2.46	3.22	2.68 [23]	2.4 [23]
Cs_2PtI_6	0.64	1.53	2.19	0.54	1.39	2.05	1.39 [95]	1.4 [24]
Cs_2PtBr_6	1.41	2.48	3.30	1.35	2.37	3.19	2.33 [95]	
Cs_2PtCl_6	2.01	3.11	3.89	1.83	2.91	3.69	3.31 [95]	
MAE	0.72	0.24	0.85	0.81	0.22	0.75	0.19	

[a]Band gap values are extracted from the band structures.
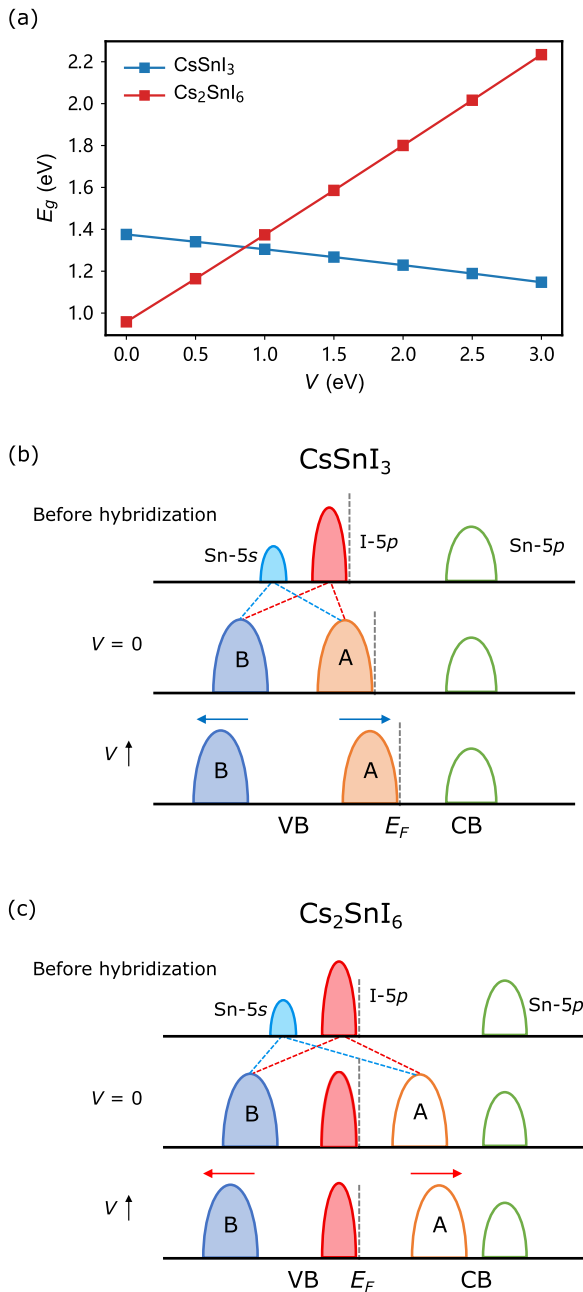
FIG. 8. Effects of Hubbard V interactions on the band gaps of $CsSnI_3$ and Cs_2SnI_6. (a) Evolution of the band gaps as a function of Hubbard V. Schematic diagram of the Sn-$5s$ and I-$5p$ energy levels in (b) $CsSnI_3$ and (c) Cs_2SnI_6 before (top panel) and after (middle and bottom panels) hybridization. The antibonding and bonding bands are labeled as A and B, respectively. In $CsSnI_3$, the band gap is mostly determined by the energy difference between the occupied antibonding states and the empty Sn-$5p$ states. A larger V that enhances the s-p hybridization will effectively push up the energy of antibonding states thus reducing the band gap. In Cs_2SnI_6, the VBM is dominated by states of I-$5p$ characters that are insensitive to V. A larger V will push up the antibonding states and increase the band gap.

antibonding states are occupied and the VBM is composed of antibonding states; the band gap is determined by the energy difference between the occupied antibonding states and the empty Sn-$5p$ states. The intersite V parameter measures the strength of hybridization between neighboring Hubbard sites. Therefore, a stronger hybridization between Sn-$5s$ and I-$5p$ will increase the bonding-antibonding energy splitting that effectively pushes up the VBM and leads to a smaller band gap [Fig. 8(b)]. In comparison, previous studies [13,35] have confirmed that the VBM of Cs_2SnI_6 is formed by the antibonding states between I-$5p$ orbitals that are nonbonding to Sn, whereas the CBM is composed of the antibonding states arising from the hybridization between Sn-$5s$ orbitals and $[I_6]$ a_{1g} molecular orbitals. It is then not surprising that the VBM is not sensitive to V while a larger V will push the CBM up and increase the band gap [Fig. 8(c)]. The enhanced stability of Cs_2SnI_6 relative to $CsSnI_3$ can thus be understood as the depletion of antibonding states rather than Sn ions acquiring a higher oxidation state of +4. Differently from $CsSnI_3$ that has a small (negative) slope of the E_g-V line, the band gap of Cs_2SnI_6 is more sensitive to Hubbard V, indicating that the Sn-I bonds in this VODP are much more covalent.

D. Electronic structures of BDHPs

The structures of two typical BDHPs, $CsTlCl_3$ and $CsAuCl_3$, are shown in Fig. 9. Both compounds have breathing-mode distortions of the halide octahedra that lead to two different local environments (DLEs) associated with the same B element. In the unit cell of $CsTlCl_3$ (space group $Fm\bar{3}m$), the $TlCl_6$ cages are alternately dilated and contracted isotropically, with Tl-Cl bonds in each individual cage being of the same length. The crystal structure of $CsAuCl_3$ has alternately compressed and elongated $[AlCl_6]$ cages along the c axis. Following the suggestions in Refs. [33,34], we label the B-site cations based on the bond geometry instead of formal oxidation state to avoid the misinterpretation of charge ordering/disproportion, that is, B^L and B^S for a B atom in a large and small octahedron, respectively. The smaller $[Cl_6]$ cage in $CsAuCl_3$ is also strongly elongated along the c axis, and the two symmetry-inequivalent Cl atoms are labeled as Cl^a for the axial site and Cl^e for the equatorial site [Fig. 9(b)].

We compute the band gaps of $CsTlCl_3$ and $CsAuCl_3$ using PBE, ACBN0, and eACBN0, and compare them with HSE and/or experimental values if available (Table IV). For $CsTlCl_3$, ACBN0 improves upon PBE, yielding a band gap of 1.50 eV, and eACBN0 further increases the band gap to 1.89 eV that is higher than the HSE value of 1.3 eV but compares favorably with the experimental value of 2.5 eV. With regard to $CsTlF_3$, we observe a similar trend: the eACBN0 band gap of 3.10 eV is larger than the ACBN0 band gap of 2.64 eV but smaller than the HSE value of 3.9 eV. Interestingly for $CsAuCl_3$, PBE and ACBN0 predict similar band gaps (0.95 versus 0.90 eV), while eACBN0 gives a band gap of 1.37 eV that is lower than the HSE value of 1.51 eV and experimental value of 2.04 eV. Overall, it is critical to take into account the hybridizations between B-site cations and halides to achieve better descriptions of the electronic structures of BDHPs.
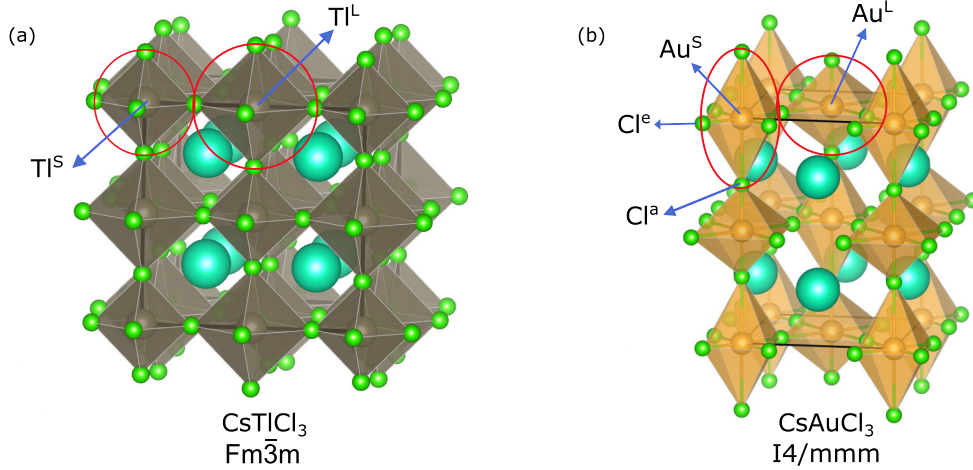
FIG. 9. Crystal structure of (a) cubic CsTlCl$_3$ in the space group of $Fm\bar{3}m$ and (b) tetragonal CsAuCl$_3$ in the space group of $I4/mmm$. Because of the breathing-mode distortions of halide octahedra, there are two different local environments (DLEs) associated with the same B element. The Tl atoms in large and small halide cages are labeled as Tl^L and Tl^S, respectively. The same notations are used for Au^L and Au^S. The smaller [Cl$_6$] cage in CsAuCl$_3$ is also strongly elongated along the c axis, and the two symmetry-inequivalent Cl atoms are labeled as Cl^a for the axial site and Cl^e for the equatorial site.

The observation that ACBN0 and PBE predict nearly the same band gap values for CsAuCl$_3$ is puzzling. We perform a detailed analysis by gradually introducing self-consistent U corrections to different orbitals. It is found that applying U_d of 2.23 eV to Au^L-5d states slightly increases the band gap to 1.09 eV [Fig. 10(a)], mainly due to the downshift of the VBM that has Au^L-5d character. In comparison, applying Hubbard U to the 5d states of Au^S atoms reduces the band gap to 0.85 eV caused by the downshift of the CBM that comprises Au^S-5d states [Fig. 10(b)]. When the Hubbard U corrections are applied to both Au^L-5d and Au^S-5d states, their effects on the band gap cancel out each other. Similar canceling effect is also found for Cl^a-3p and Cl^e-3p [see Figs. 10(c) and 10(d)]. Consequently, the collective Hubbard U corrections to 5d states of Au and 3p states of Cl, though strongly affecting the DOS spectrum, do not change the band gap appreciably [Fig. 10(e)]. It is only after the application of intersite V corrections that the band gap increases due to the upshift of the CBM [Fig. 10(f)].

E. Effects of Hubbard V interactions in BDHPs

The inclusion of the intersite Hubbard V is crucial to properly capture the hybridization between valence electrons on neighboring atoms in BDHPs. A detailed understanding of the effects of V is therefore worthy of investigations. There are four nonequivalent Au-Cl bonds in CsAuCl$_3$ with $r(\text{Au}^L\text{-Cl}^a) < r(\text{Au}^S\text{-Cl}^e) < r(\text{Au}^L\text{-Cl}^e) < r(\text{Au}^S\text{-Cl}^a)$, corresponding to different degrees of hybridizations and four V parameters (Table V). A set of model calculations reveals that the band gap of CsAuCl$_3$ opens up with increasing $V(\text{Au}^S\text{-Cl}^e)$, but decreases with increasing $V(\text{Au}^L\text{-Cl}^a)$, while being insensitive to both $V(\text{Au}^L\text{-Cl}^e)$ and $V(\text{Au}^S\text{-Cl}^a)$. That is, the electronic structure is more sensitive to the intersite V parameters of two shorter bonds. The trend can be understood with the diagram illustrated in Fig. 11. The hybridization between Au-5d and Cl-3p orbitals leads to the splitting between the bonding and antibonding states. Because of the presence of two DLEs and the associated differing strengths in hybridization, the antibonding states (denoted as A^S) resulting from Au-5d and Cl-3p orbitals of the smaller [AuCl$_6$] cage are higher in energy and are unoccupied; the antibonding states (denoted as A^L) resulting from Au-Cl hybridizations in the larger [AuCl$_6$] cage are occupied and contribute to the VBM. As a result, a large $V(\text{Au}^S\text{-Cl}^e)$ will push up the CBM and increase the band gap, while an increase in $V(\text{Au}^L\text{-Cl}^a)$ will upshift the VBM and cause a gap reduction. A similar trend is also found in CsTlF$_3$ and CsTlCl$_3$ as well. For example, CsTlF$_3$ has the band gap increasing with increasing $V(\text{Tl}^S\text{-F})$.

TABLE IV. Comparison of the band gaps (in eV) as computed with different methods and as measured in experiments for BDHPs. The sc-eACBN0 method simultaneously converges both structure and Hubbard U and V parameters.

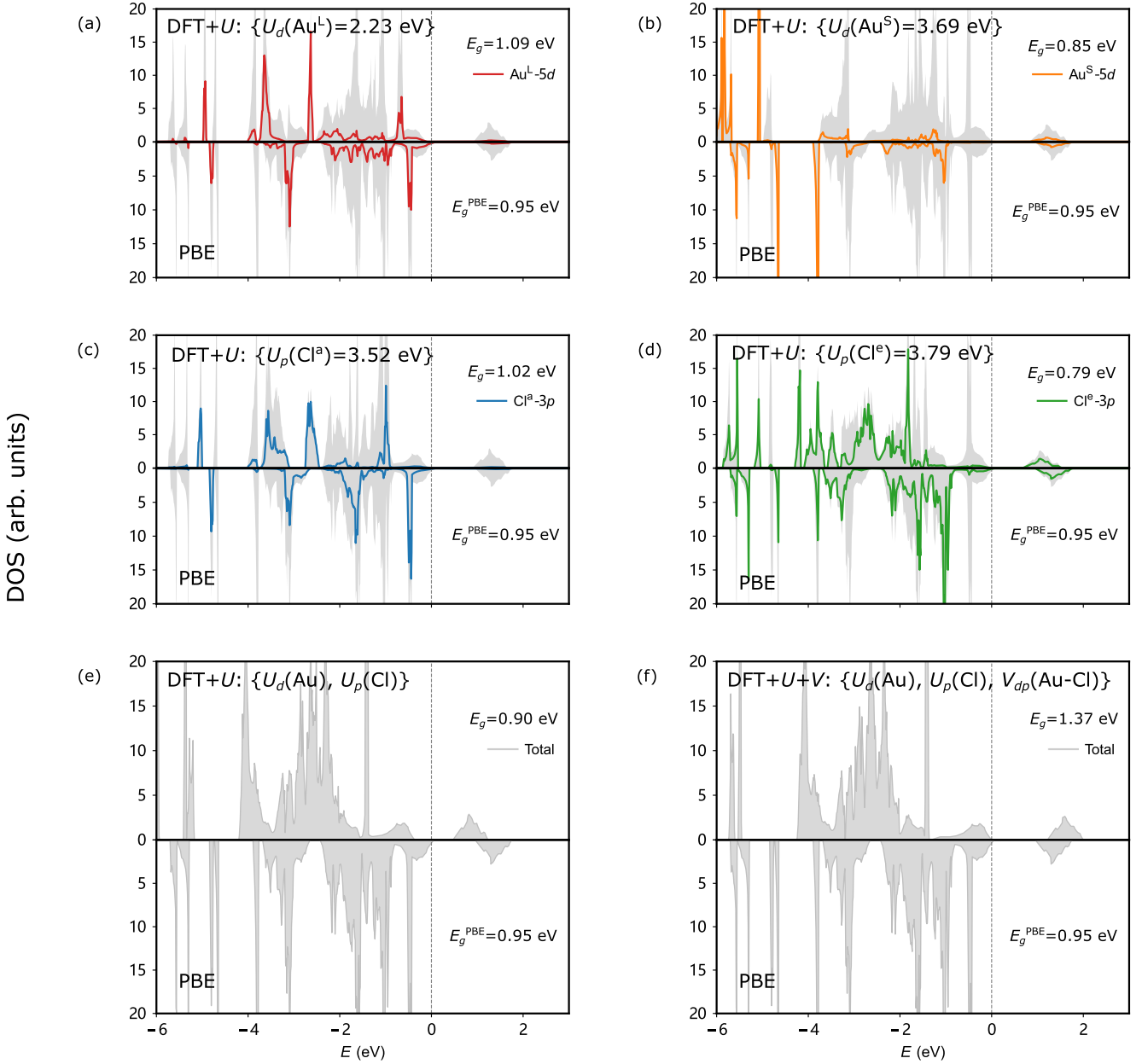|	This Work				Reference	
	PBE	ACBN0	eACBN0	sc-eACBN0	HSE	Expt.
CsTlCl$_3$	1.00	1.50	1.89	2.67	1.3 [26]	2.5 [26]
CsTlF$_3$	2.15	2.64	3.10	4.46	3.9 [26]	
CsAuCl$_3$	0.95	0.90	1.37	1.73	1.51 [33]	2.04 [29]

FIG. 10. Diagnostic analysis of Hubbard U and V corrections in CsAuI$_3$. Comparison of density of states computed with PBE and those computed with self-consistent Hubbard U corrections applied to (a) Au^L-5d states, (b) Au^S-5d states, (c) Cl^a-3p states, (d) Cl^e-3p states, and (e) both Au-5d and Cl-3p states. Both U and V correlations are included in (f) that clearly shows an upshift of the CBM in eACBN0.

It is evident that the band gaps of BDHPs depend on the relative hybridization strength between two DLEs. A recent work [69] shows that the self-consistent Hubbard V plays a decisive role in describing the coupled charge and lattice degrees of freedom in charge-ordered systems such as Ba$_{1-x}$K$_x$AO$_3$ (A = Bi and Sb) [69]. So far, we obtain self-consistent U and V parameters for a given structure optimized with PBE. This then raises a few important questions: Is it possible to converge both Hubbard parameters as well as crystal geometry at the same time? How large an impact will this have on the electronic structure? To address these questions, we follow a protocol developed in Ref. [70] that

drives the system to the ground state while fully accounting for the changes in the Hubbard parameters. The major difference between our protocol (termed sc-eACBN0) in Fig. 12 and that in Ref. [70] is that we use eACBN0 instead of density functional perturbation theory to compute Hubbard parameters self-consistently [71]. The band gaps and converged Hubbard parameters are reported in Tables IV and V. Interestingly, the band gap prediction of sc-eACBN0 improves greatly over eACBN0. For example, sc-eACBN0 gives a band gap of 2.67 eV for CsTlCl$_3$ and 1.73 eV for CsAuCl$_3$, both in reasonable agreement with experimental values of 2.5 and 2.04 eV, respectively. Structurally, the equilibrium lattice

TABLE V. Self-consistent U and V values (in eV) for different orbitals in $CsAuCl_3$ computed with ACBN0, eACBN0, and sc-eACBN0. V_{dp} is the intersite Hubbard term between nearest-neighboring Au-$5d$ and Cl-$3p$ orbitals. Underlined Hubbard parameters are most important for band gap predictions.

	$CsAuCl_3$		
U/V Values	ACBN0	eACBN0	sc-eACBN0
$U(Cs\text{-}6s)$	0.00	0.00	0.00
$U(Cs\text{-}5p)$	2.87	2.85	2.39
$U(Au^L\text{-}6s)$	0.11	0.15	0.22
$\underline{U(Au^L\text{-}5d)}$	2.23	2.35	2.59
$U(Au^S\text{-}6s)$	0.05	0.06	0.06
$\underline{U(Au^S\text{-}5d)}$	3.69	3.49	3.53
$\underline{U(Cl^a\text{-}3p)}$	3.42	3.44	3.52
$\underline{U(Cl^e\text{-}3p)}$	3.60	3.65	3.79
$\underline{V_{dp}(Au^L\text{-}Cl^a)}$		2.56	2.59
$\underline{V_{dp}(Au^L\text{-}Cl^e)}$		1.96	1.88
$\underline{V_{dp}(Au^S\text{-}Cl^a)}$		1.68	1.67
$\underline{V_{dp}(Au^S\text{-}Cl^e)}$		2.32	2.35

constants and Au-Cl bond lengths obtained with sc-eACBN0 are $\approx 1.7\%$ larger than the corresponding PBE values (Table VI). Such "structural dilation" has been previously observed for $LiMnPO_4$ and $MnPO_4$ that DFT $+ U + V$ predicts larger lattice constants than standard DFT [70]. Overall, we believe sc-eACBN0 is a cost-effective and accurate approach to predict the electronic structures of BDHPs. To serve as a complete test, we further optimize the structures of $CsSnI_3$ and Cs_2SnI_6 with sc-ACBN0. We again observe a "structural dilation" effect: The sc-eACBN0 lattice constants are larger than their PBE values by $+1.4\%$ and $+1.2\%$ for $CsSnI_3$ and Cs_2SnI_6, respectively. In comparison with eACBN0 band gaps, sc-eACBN0 band gaps only increase by 0.2 eV for both compounds, implying that the band gaps of ABX_3-type HPs and VODPs are less sensitive to structural perturbations than BDHPs.

IV. CONCLUSION

The vast diversity of chemical space enabled by HPs opens up exciting opportunities to obtain novel materials with highly tunable electronic properties for a broad range of applications. It is desirable to have a fully *ab initio* method to accurately predict the electronic structures of HPs with minimum hu-

TABLE VI. Theoretical and experimental lattice constants and Au-Cl bond lengths (in Å) of $CsAuCl_3$.

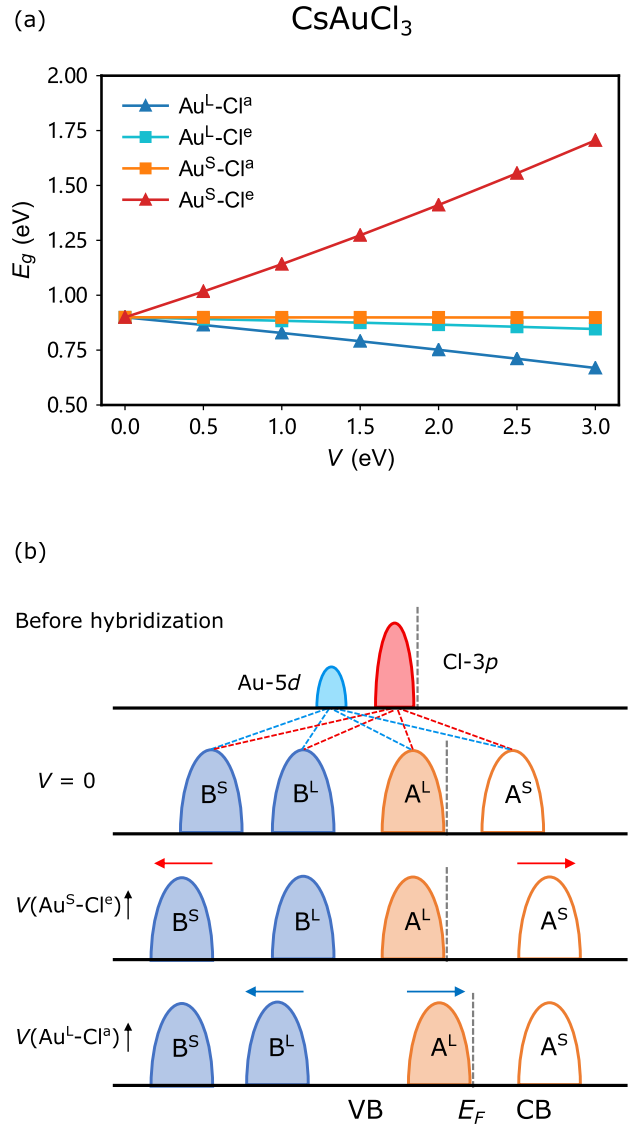|	PBE	sc-eACBN0	Previous Work [96]	Expt. [97]
a	7.62	7.82	7.6037	7.495
c	11.31	11.39	11.251	10.880
$Au^L\text{-}Cl^a$	2.31	2.31	2.314	2.28
$Au^L\text{-}Cl^e$	3.04	3.19	3.018	3.01
$Au^S\text{-}Cl^a$	3.34	3.38	3.311	3.15
$Au^S\text{-}Cl^e$	2.35	2.33	2.359	2.29

FIG. 11. Effects of Hubbard V interactions on the band gaps of $CsAuCl_3$. (a) Evolution of the band gaps as a function of Hubbard V. There are four nonequivalent Au-Cl bonds in $CsAuCl_3$, corresponding to four V parameters. $Au^S\text{-}Cl^e$ and $Au^L\text{-}Cl^a$ are the shortest two bonds. (b) Schematic diagram of the Au-$5d$ and Cl-$3p$ energy levels before (top panel) and after hybridization. The hybridization between Au-$5d$ and Cl-$3p$ orbitals leads to the splitting between the bonding and antibonding states. The antibonding bands resulting from d-p hybridization of the smaller $[AuCl_6]$ cage, denoted as A^S, are higher in energy and are unoccupied, while the antibonding bands labeled as A^L contribute to the VBM. A larger $V(Au^S\text{-}Cl^e)$ will push up A^S and increase the band gap, while an increase in $V(Au^L\text{-}Cl^a)$ will upshift A^L and cause a band gap reduction.

man bias and affordable computational expense. In this work, we investigate three different types of HPs that have drastically different bonding characters using DFT $+ U$ and DFT $+ U + V$ with onsite U and intersite V Hubbard parameters computed self-consistently without *ad hoc* assumption. We demonstrate that ACBN0 and eACBN0, a DFT $+ U$ method
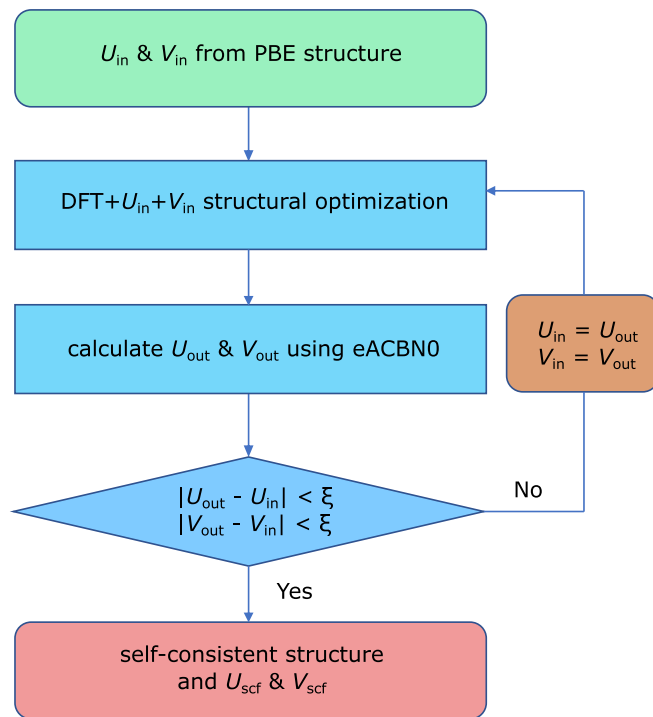
FIG. 12. Flow chart of sc-eACBN0 that converges both geometry and Hubbard parameters.

and its extended version with V, have improved band gap prediction accuracy over PBE and on par with HSE/GW. Specifically, the finding that the $5s$ electrons of Sn in CsSnI$_3$ and Cs$_2$SnI$_6$ acquire similar on-site Hubbard U values supports the mechanism of charge self-regulating response: Sn ions in these two compounds actually have comparable charge states. This highlights that the self-consistent U that depends sensitively on the local atomic environment can serve as a useful indicator of the true charge state. Moreover, the simultaneous convergence of both Hubbard parameters and crystal geometry enables a band gap prediction accuracy superior to HSE for bond disproportionated halide perovskites that have complex distortions of the halide octahedra. Our work paves the way for future studies of complex compounds beyond HPs containing localized electrons that often possess intricate competitions between onsite localization and intersite hybridization.

[1] A. Kojima, K. Teshima, Y. Shirai, and T. Miyasaka, Organometal halide perovskites as visible-light sensitizers for photovoltaic cells, J. Am. Chem. Soc. **131**, 6050 (2009).

[2] M. M. Lee, J. Teuscher, T. Miyasaka, T. N. Murakami, and H. J. Snaith, Efficient hybrid solar cells based on meso-superstructured organometal halide perovskites, Science **338**, 643 (2012).

[3] N. J. Jeon, J. H. Noh, W. S. Yang, Y. C. Kim, S. Ryu, J. Seo, and S. I. Seok, Compositional engineering of perovskite materials for high-performance solar cells, Nature (London) **517**, 476 (2015).

[4] M. A. Green, E. D. Dunlop, J. Hohl-Ebinger, M. Yoshita, N. Kopidakis, and X. Hao, Solar cell efficiency tables (version 59), Prog. Photovoltaics **30**, 3 (2022).

[5] J. H. Noh, S. H. Im, J. H. Heo, T. N. Mandal, and S. I. Seok, Chemical management for colorful, efficient, and stable inorganic-organic hybrid nanostructured solar cells, Nano Lett. **13**, 1764 (2013).

[6] W.-J. Yin, T. Shi, and Y. Yan, Unique properties of halide perovskites as possible origins of the superior solar cell performance, Adv. Mater. **26**, 4653 (2014).

[7] J.-P. Correa-Baena, M. Saliba, T. Buonassisi, M. Grätzel, A. Abate, W. Tress, and A. Hagfeldt, Promises and challenges of perovskite solar cells, Science **358**, 739 (2017).

[8] M. Saliba, Perovskite solar cells must come of age, Science **359**, 388 (2018).

[9] J. Im, S. Lee, T.-W. Ko, H. W. Kim, Y. Hyon, and H. Chang, Identifying Pb-free perovskites for solar cells by machine learning, npj Comput. Mater. **5**, 37 (2019).

[10] T. Wu, X. Liu, X. Luo, X. Lin, D. Cui, Y. Wang, H. Segawa, Y. Zhang, and L. Han, Lead-free tin perovskite solar cells, Joule **5**, 863 (2021).

[11] Z. Xiao, Z. Song, and Y. Yan, From lead halide perovskites to lead-free metal halide perovskites and perovskite derivatives, Adv. Mater. **31**, 1803792 (2019).

[12] B. Lee, C. C. Stoumpos, N. Zhou, F. Hao, C. Malliakas, C.-Y. Yeh, T. J. Marks, M. G. Kanatzidis, and R. P. Chang, Air-stable molecular semiconducting iodosalts for solar cell applications: Cs$_2$SnI$_6$ as a hole conductor, J. Am. Chem. Soc. **136**, 15379 (2014).

[13] Z. Xiao, H. Lei, X. Zhang, Y. Zhou, H. Hosono, and T. Kamiya, Ligand-hole in [SnI$_6$] unit and origin of band gap in photovoltaic perovskite variant Cs$_2$SnI$_6$, Bull. Chem. Soc. Jpn. **88**, 1250 (2015).

[14] A. E. Maughan, A. M. Ganose, D. O. Scanlon, and J. R. Neilson, Perspectives and design principles of vacancy-ordered double perovskite halide semiconductors, Chem. Mater. **31**, 1184 (2019).

[15] A. Kaltzoglou, M. Antoniadou, A. G. Kontos, C. C. Stoumpos, D. Perganti, E. Siranidi, V. Raptis, K. Trohidou, V. Psycharis, M. G. Kanatzidis *et al.*, Optical-vibrational properties of the Cs$_2$SnX$_6$ (X = Cl, Br, I) defect perovskites and hole-transport efficiency in dye-sensitized solar cells, J. Phys. Chem. C **120**, 11777 (2016).

[16] A. E. Maughan, A. M. Ganose, M. M. Bordelon, E. M. Miller, D. O. Scanlon, and J. R. Neilson, Defect tolerance to intolerance in the vacancy-ordered double perovskite semiconductors Cs$_2$SnI$_6$ and Cs$_2$TeI$_6$, J. Am. Chem. Soc. **138**, 8453 (2016).

[17] M. C. Folgueras, J. Jin, M. Gao, L. N. Quan, J. A. Steele, S. Srivastava, M. B. Ross, R. Zhang, F. Seeler, K. Schierle-Arndt *et al.*, Lattice dynamics and optoelectronic properties of vacancy-ordered double perovskite Cs$_2$TeX$_6$ (X = Cl$^-$, Br$^-$, I$^-$) single crystals, J. Phys. Chem. C **125**, 25126 (2021).

[18] M.-G. Ju, M. Chen, Y. Zhou, H. F. Garces, J. Dai, L. Ma, N. P. Padture, and X. C. Zeng, Earth-abundant nontoxic titanium (IV)-based vacancy-ordered double perovskite halides with tunable 1.0 to 1.8 eV bandgaps for photovoltaic applications, ACS Energy Lett. **3**, 297 (2018).

[19] D. Kong, D. Cheng, X. Wang, K. Zhang, H. Wang, K. Liu, H. Li, X. Sheng, and L. Yin, Solution processed lead-free cesium titanium halide perovskites and their structural, thermal and optical characteristics, J. Mater. Chem. C **8**, 1591 (2020).

[20] A. Abfalterer, J. Shamsi, D. J. Kubicki, C. N. Savory, J. Xiao, G. Divitini, W. Li, S. Macpherson, K. Gałkowski, J. L. MacManus-Driscoll *et al.*, Colloidal synthesis and optical properties of perovskite-inspired cesium zirconium halide nanocrystals, ACS Mater. Lett. **2**, 1644 (2020).

[21] L. Zhou, J.-F. Liao, Z.-G. Huang, X.-D. Wang, Y.-F. Xu, H.-Y. Chen, D.-B. Kuang, and C.-Y. Su, All-inorganic lead-free Cs_2PdX_6 (X = Br, I) perovskite nanocrystals with single unit cell thickness and high stability, ACS Energy Lett. **3**, 2613 (2018).

[22] N. Sakai, A. A. Haghighirad, M. R. Filip, P. K. Nayak, S. Nayak, A. Ramadan, Z. Wang, F. Giustino, and H. J. Snaith, Solution-processed cesium hexabromopalladate (IV), Cs_2PdBr_6, for optoelectronic applications, J. Am. Chem. Soc. **139**, 6030 (2017).

[23] Z.-Y. Wang, Y. Chen, C. Zhang, D. Wang, P. Liang, H. Zhang, R.-J. Xie, and L. Wang, Electronic structure and optical properties of vacancy-ordered double perovskites $Cs_2PdBr_xCl_{6-x}$ by first-principles calculation, J. Phys. Chem. C **124**, 13310 (2020).

[24] D. Schwartz, R. Murshed, H. Larson, B. Usprung, S. Soltanmohamad, R. Pandey, E. S. Barnard, A. Rockett, T. Hartmann, I. E. Castelli *et al.*, Air stable, high-efficiency, Pt-based halide perovskite solar cells with long carrier lifetimes, Phys. Status Solidi RRL **14**, 2000182 (2020).

[25] N. Matsushita, H. Ahsbahs, S. S. Hafner, and N. Kojima, Single crystal x-ray diffraction study of a mixed-valence gold compound, $Cs_2Au^IAu^{III}Cl_6$, under high pressures up to 18 GPa: Pressure-induced phase transition coupled with gold valence transition, J. Solid State Chem. **180**, 1353 (2007).

[26] M. Retuerto, T. Emge, J. Hadermann, P. W. Stephens, M. R. Li, Z. P. Yin, M. Croft, A. Ignatov, S. J. Zhang, Z. Yuan, C. Jin, J. W. Simonson, M. C. Aronson, A. Pan, D. N. Basov, G. Kotliar, and M. Greenblatt, Synthesis and properties of charge-ordered thallium halide perovskites, $CsTl^+_{0.5}Tl^{3+}_{0.5}X_3$ (X = F or Cl): Theoretical precursors for superconductivity?, Chem. Mater. **25**, 4071 (2013).

[27] C. M. Varma, Missing Valence States, Diamagnetic Insulators, and Superconductors, Phys. Rev. Lett. **61**, 2713 (1988).

[28] I. Hase and T. Yanagisawa, Madelung energy of the valence-skipping compound $BaBiO_3$, Phys. Rev. B **76**, 174103 (2007).

[29] X. J. Liu, K. Matsuda, Y. Moritomo, A. Nakamura, and N. Kojima, Electronic structure of the gold complexes $Cs_2Au_2X_6$ (X = I, Br, and Cl), Phys. Rev. B **59**, 7925 (1999).

[30] S. Wang, S. Hirai, M. C. Shapiro, S. C. Riggs, T. H. Geballe, W. L. Mao, and I. R. Fisher, Pressure-induced symmetry breaking in tetragonal $CsAuI_3$, Phys. Rev. B **87**, 054104 (2013).

[31] J. Lin, H. Chen, Y. Gao, Y. Cai, J. Jin, A. S. Etman, J. Kang, T. Lei, Z. Lin, M. C. Folgueras, L. N. Quan, Q. Kong, M. Sherburne, M. Asta, J. Sun, M. F. Toney, J. Wu, and P. Yang, Pressure-induced semiconductor-to-metal phase transition of a charge-ordered indium halide perovskite, Proc. Natl. Acad. Sci. USA **116**, 23404 (2019).

[32] H. Raebiger, S. Lany, and A. Zunger, Charge self-regulation upon changing the oxidation state of transition metals in insulators, Nature (London) **453**, 763 (2008).

[33] G. M. Dalpian, Q. Liu, J. Varignon, M. Bibes, and A. Zunger, Bond disproportionation, charge self-regulation, and ligand holes in *s-p* and in *d*-electron ABX_3 perovskites by density functional theory, Phys. Rev. B **98**, 075135 (2018).

[34] M. R. Benam, K. Foyevtsova, A. Khazraie, I. Elfimov, and G. A. Sawatzky, Bond versus charge disproportionation and nature of the holes in *s-p* ABX_3 perovskites, Phys. Rev. B **104**, 195141 (2021).

[35] G. M. Dalpian, Q. Liu, C. C. Stoumpos, A. P. Douvalis, M. Balasubramanian, M. G. Kanatzidis, and A. Zunger, Changes in charge density vs changes in formal oxidation states: The case of Sn halide perovskites and their ordered vacancy analogues, Phys. Rev. Mater. **1**, 025401 (2017).

[36] J. Even, L. Pedesseau, J.-M. Jancu, and C. Katan, Importance of spin-orbit coupling in hybrid organic/inorganic perovskites for photovoltaic applications, J. Phys. Chem. Lett. **4**, 2999 (2013).

[37] E. Mosconi, A. Amat, M. K. Nazeeruddin, M. Grätzel, and F. De Angelis, First-principles modeling of mixed halide organometal perovskites for photovoltaic applications, J. Phys. Chem. C **117**, 13902 (2013).

[38] T. Das, G. Di Liberto, and G. Pacchioni, Density functional theory estimate of halide perovskite band gap: When spin orbit coupling helps, J. Phys. Chem. C **126**, 2184 (2022).

[39] P. Mori-Sánchez, A. J. Cohen, and W. Yang, Many-electron self-interaction error in approximate density functionals, J. Chem. Phys. **125**, 201102 (2006).

[40] J. P. Perdew and Y. Wang, Accurate and simple analytic representation of the electron-gas correlation energy, Phys. Rev. B **45**, 13244 (1992).

[41] J. P. Perdew, K. Burke, and M. Ernzerhof, Generalized Gradient Approximation Made Simple, Phys. Rev. Lett. **77**, 3865 (1996).

[42] H. J. Kulik, Perspective: Treating electron over-delocalization with the DFT + U method, J. Chem. Phys. **142**, 240901 (2015).

[43] J. P. Perdew and M. Levy, Physical Content of the Exact Kohn-Sham Orbital Energies: Band Gaps and Derivative Discontinuities, Phys. Rev. Lett. **51**, 1884 (1983).

[44] M. Cococcioni and S. de Gironcoli, Linear response approach to the calculation of the effective interaction parameters in the LDA+U method, Phys. Rev. B **71**, 035105 (2005).

[45] L. A. Agapito, S. Curtarolo, and M. Buongiorno Nardelli, Reformulation of DFT + U as a Pseudohybrid Hubbard Density Functional for Accelerated Materials Discovery, Phys. Rev. X **5**, 011006 (2015).

[46] V. Leiria Campo Jr. and M. Cococcioni, Extended DFT + U + V method with on-site and inter-site electronic interactions, J. Phys.: Condens. Matter **22**, 055602 (2010).

[47] S.-H. Lee and Y.-W. Son, First-principles approach with a pseudohybrid density functional for extended Hubbard interactions, Phys. Rev. Res. **2**, 043410 (2020).

[48] N. Tancogne-Dejean and A. Rubio, Parameter-free hybridlike functional based on an extended Hubbard model: DFT+U + V, Phys. Rev. B **102**, 155117 (2020).

[49] P. Giannozzi, S. Baroni, N. Bonini, M. Calandra, R. Car, C. Cavazzoni, D. Ceresoli, G. L. Chiarotti, M. Cococcioni, I. Dabo *et al.*, QUANTUM ESPRESSO: A modular and open-source

software project for quantum simulations of materials, J. Phys.: Condens. Matter **21**, 395502 (2009).

[50] P. Giannozzi, O. Andreussi, T. Brumme, O. Bunau, M. B. Nardelli, M. Calandra, R. Car, C. Cavazzoni, D. Ceresoli, M. Cococcioni *et al.*, Advanced capabilities for materials modelling with QUANTUM ESPRESSO, J. Phys.: Condens. Matter **29**, 465901 (2017).

[51] K. F. Garrity, J. W. Bennett, K. M. Rabe, and D. Vanderbilt, Pseudopotentials for high-throughput DFT calculations, Comput. Mater. Sci. **81**, 446 (2014).

[52] N. E. Kirchner-Hall, W. Zhao, Y. Xiong, I. Timrov, and I. Dabo, Extensive benchmarking of DFT + U calculations for predicting band gaps, Appl. Sci. **11**, 2395 (2021).

[53] M. J. van Setten, M. Giantomassi, E. Bousquet, M. J. Verstraete, D. R. Hamann, X. Gonze, and G.-M. Rignanese, The pseudodojo: Training and grading a 85 element optimized norm-conserving pseudopotential table, Comput. Phys. Commun. **226**, 39 (2018).

[54] S. L. Dudarev, G. A. Botton, S. Y. Savrasov, C. J. Humphreys, and A. P. Sutton, Electron-energy-loss spectra and the structural stability of nickel oxide: An LSDA+U study, Phys. Rev. B **57**, 1505 (1998).

[55] I. Timrov, F. Aquilante, L. Binci, M. Cococcioni, and N. Marzari, Pulay forces in density-functional theory with extended Hubbard functionals: From nonorthogonalized to orthogonalized manifolds, Phys. Rev. B **102**, 235159 (2020).

[56] P.-O. Löwdin, On the non-orthogonality problem connected with the use of atomic wave functions in the theory of molecules and crystals, J. Chem. Phys. **18**, 365 (1950).

[57] See https://github.com/sliutheorygroup/supplementary-material/tree/main/L47.

[58] J. Yang, T. Zhu, and S. Liu, Onsite and intersite electronic correlations in the Hubbard model for halide perovskites, Materials Cloud Archive 2022.135, doi:10.24435/materialscloud:wt-91, (2022).

[59] K. J. May and A. M. Kolpak, Improved description of perovskite oxide crystal structure and electronic properties using self-consistent Hubbard U corrections from ACBN0, Phys. Rev. B **101**, 165117 (2020).

[60] P. Gopal, M. Fornari, S. Curtarolo, L. A. Agapito, L. S. I. Liyanage, and M. B. Nardelli, Improved predictions of the physical properties of Zn- and Cd-based wide band-gap semiconductors: A validation of the ACBN0 functional, Phys. Rev. B **91**, 245202 (2015).

[61] M. Yu, S. Yang, C. Wu, and N. Marom, Machine learning the Hubbard U parameter in DFT + U using Bayesian optimization, npj Comput. Mater. **6**, 180 (2020).

[62] J. Huang, S.-H. Lee, Y.-W. Son, A. Supka, and S. Liu, First-principles study of two-dimensional ferroelectrics using self-consistent Hubbard parameters, Phys. Rev. B **102**, 165157 (2020).

[63] C. Ke, J. Huang, and S. Liu, Two-dimensional ferroelectric metal for electrocatalysis, Mater. Horiz. **8**, 3387 (2021).

[64] B. Cucco, G. Bouder, L. Pedesseau, C. Katan, J. Even, M. Kepenekian, and G. Volonakis, Electronic structure and stability of Cs_2TiX_6 and Cs_2ZrX_6 (X = Br, I) vacancy ordered double perovskites, Appl. Phys. Lett. **119**, 181903 (2021).

[65] M. van Schilfgaarde, T. Kotani, and S. Faleev, Quasiparticle Self-Consistent *GW* Theory, Phys. Rev. Lett. **96**, 226402 (2006).

[66] M. Shishkin, M. Marsman, and G. Kresse, Accurate Quasiparticle Spectra from Self-Consistent *GW* Calculations with Vertex Corrections, Phys. Rev. Lett. **99**, 246403 (2007).

[67] L. Sponza, V. Véniard, F. Sottile, C. Giorgetti, and L. Reining, Role of localized electrons in electron-hole interaction: The case of $SrTiO_3$, Phys. Rev. B **87**, 235102 (2013).

[68] L. Chiodo, J. M. García-Lastra, A. Iacomino, S. Ossicini, J. Zhao, H. Petek, and A. Rubio, Self-energy and excitonic effects in the electronic and optical properties of TiO_2 crystalline phases, Phys. Rev. B **82**, 045207 (2010).

[69] B. G. Jang, M. Kim, S.-H. Lee, W. Yang, S.-H. Jhi, and Y.-W. Son, Decisive roles of intersite Coulomb interactions in charge ordered systems, arXiv:2205.02470.

[70] I. Timrov, N. Marzari, and M. Cococcioni, Self-consistent Hubbard parameters from density-functional perturbation theory in the ultrasoft and projector-augmented wave formulations, Phys. Rev. B **103**, 045141 (2021).

[71] I. Timrov, N. Marzari, and M. Cococcioni, Hubbard parameters from density-functional perturbation theory, Phys. Rev. B **98**, 085127 (2018).

[72] L. Y. Huang and W. R. L. Lambrecht, Electronic band structure, phonons, and exciton binding energies of halide perovskites $CsSnCl_3$, $CsSnBr_3$, and $CsSnI_3$, Phys. Rev. B **88**, 165203 (2013).

[73] Z. Chen, C. Yu, K. Shum, J. J. Wang, W. Pfenninger, N. Vockic, J. Midgley, and J. T. Kenney, Photoluminescence study of polycrystalline $CsSnI_3$ thin films: Determination of exciton binding energy, J. Lumin. **132**, 345 (2012).

[74] S. J. Clark, C. D. Flint, and J. D. Donaldson, Luminescence and electrical conductivity of $CsSnBr_3$, and related phases, J. Phys. Chem. Solids **42**, 133 (1981).

[75] L. Peedikakkandy and P. Bhargava, Composition dependent optical, structural and photoluminescence characteristics of cesium tin halide perovskites, RSC Adv. **6**, 19857 (2016).

[76] A. Voloshinovskii, S. Myagkota, N. Pidzyrailo, and M. Tokarivskii, Luminescence and structural transformations of $CsSnCl_3$ crystals, J. Appl. Spectrosc. **60**, 226 (1994).

[77] P. Umari, E. Mosconi, and F. De Angelis, Relativistic *GW* calculations on $CH_3NH_3PbI_3$ and $CH_3NH_3SnI_3$ perovskites for solar cell applications, Sci. Rep. **4**, 4467 (2014).

[78] C. C. Stoumpos, C. D. Malliakas, and M. G. Kanatzidis, Semiconducting tin and lead iodide perovskites with organic cations: Phase transitions, high mobilities, and near-infrared photoluminescent properties, Inorg. Chem. **52**, 9019 (2013).

[79] E. S. Parrott, R. L. Milot, T. Stergiopoulos, H. J. Snaith, M. B. Johnston, and L. M. Herz, Effect of structural phase transition on charge-carrier lifetimes and defects in $CH_3NH_3SnI_3$ perovskite, J. Phys. Chem. Lett. **7**, 1321 (2016).

[80] M. Bokdam, T. Sander, A. Stroppa, S. Picozzi, D. Sarma, C. Franchini, and G. Kresse, Role of polar phonons in the photo excited state of metal halide perovskites, Sci. Rep. **6**, 28618 (2016).

[81] Y. Dang, Y. Zhou, X. Liu, D. Ju, S. Xia, H. Xia, and X. Tao, Formation of hybrid perovskite tin iodide single crystals by top-seeded solution growth, Angew. Chem., Int. Ed. **55**, 3447 (2016).

[82] F. Chiarella, A. Zappettini, F. Licci, I. Borriello, G. Cantele, D. Ninno, A. Cassinese, and R. Vaglio, Combined experimental and theoretical investigation of optical, structural, and

electronic properties of CH$_3$NH$_3$SnX$_3$ thin films (X=Cl, Br), Phys. Rev. B **77**, 045129 (2008).

[83] R. J. Sutton, M. R. Filip, A. A. Haghighirad, N. Sakai, B. Wenger, F. Giustino, and H. J. Snaith, Cubic or orthorhombic? Revealing the crystal structure of metastable black-phase CsPbI$_3$ by theory and experiment, ACS Energy Lett. **3**, 1787 (2018).

[84] G. E. Eperon, S. D. Stranks, C. Menelaou, M. B. Johnston, L. M. Herz, and H. J. Snaith, Formamidinium lead trihalide: A broadly tunable perovskite for efficient planar heterojunction solar cells, Energy Environ. Sci. **7**, 982 (2014).

[85] J. Brgoch, A. J. Lehner, M. Chabinyc, and R. Seshadri, Ab initio calculations of band gaps and absolute band positions of polymorphs of RbPbI$_3$ and CsPbI$_3$: Implications for main-group halide perovskite photovoltaics, J. Phys. Chem. C **118**, 27721 (2014).

[86] B. Wang, N. Novendra, and A. Navrotsky, Energetics, structures, and phase transitions of cubic and orthorhombic cesium lead iodide (CsPbI$_3$) polymorphs, J. Am. Chem. Soc. **141**, 14501 (2019).

[87] L. Lang, Y.-Y. Zhang, P. Xu, S. Chen, H. J. Xiang, and X. G. Gong, Three-step approach for computing band offsets and its application to inorganic ABX$_3$ halide perovskites, Phys. Rev. B **92**, 075102 (2015).

[88] K. Gesi, K. Ozawa, and S. Hirotsu, Effect of hydrostatic pressure on the structural phase transitions in CsPbCl$_3$ and CsPbBr$_3$, J. Phys. Soc. Jpn. **38**, 463 (1975).

[89] F. Hao, C. C. Stoumpos, R. P. Chang, and M. G. Kanatzidis, Anomalous band gap behavior in mixed Sn and Pb perovskites enables broadening of absorption spectrum in solar cells, J. Am. Chem. Soc. **136**, 8094 (2014).

[90] T. Ishihara, Optical properties of PbI-based perovskite structures, J. Lumin. **60-61**, 269 (1994).

[91] L. Y. Huang and W. R. L. Lambrecht, Electronic band structure trends of perovskite halides: Beyond Pb and Sn to Ge and Si, Phys. Rev. B **93**, 195211 (2016).

[92] A. M. Leguy, P. Azarhoosh, M. I. Alonso, M. Campoy-Quiles, O. J. Weber, J. Yao, D. Bryant, M. T. Weller, J. Nelson, A. Walsh *et al.*, Experimental and theoretical optical properties of methylammonium lead halide perovskites, Nanoscale **8**, 6317 (2016).

[93] N. Pandech, T. Kongnok, N. Palakawong, S. Limpijumnong, W. R. Lambrecht, and S. Jungthawan, Effects of the van der Waals interactions on structural and electronic properties of CH$_3$NH$_3$(Pb,Sn)(I,Br,Cl)$_3$ halide perovskites, ACS Omega **5**, 25723 (2020).

[94] M. Faizan, S. H. Khan, H. Khachai, T. Seddik, S. B. Omran, R. Khenata, J. Xie, and M. m. AL-Anazy, Electronic, optical, and thermoelectric properties of perovskite variants A$_2$BX$_6$: Insight and design via first-principles calculations, Int. J. Energy Res. **45**, 4495 (2021).

[95] X. Ye, A. Liu, Y. Zhao, Q. Han, T. Kitamura, and T. Ma, DFT study of X-site ion substitution doping of Cs$_2$PtX$_6$ on its structural and electronic properties, Int. J. Energy Res. **46**, 8471 (2022).

[96] B. Winkler, C. J. Pickard, M. D. Segall, and V. Milman, Density-functional study of charge disordering in Cs$_2$Au(I)Au(III)Cl$_6$ under pressure, Phys. Rev. B **63**, 214103 (2001).

[97] W. Denner, H. Schulz, and H. d'Amour, The influence of high hydrostatic pressure on the crystal structure of cesium gold chloride (Cs$_2$Au^{I}Au^{III}Cl$_6$) in the pressure range up to 52×10^8 Pa, Acta Crystallogr., Sect. A **35**, 360 (1979).